

RESEARCH PAPER

Structural, Optical and Magnetic Characterization of Vanadium Pentoxide Nanoparticles Synthesized in a Gelatin Medium

Maliheh Mousavi¹, Shekoofeh Tabatabai Yazdi^{2*}, Gholam Hossein Khorrami¹

¹ Department of Physics, Faculty of basic sciences, University of Bojnord, Bojnord, Iran

² Department of Physics, Payame Noor University (PNU), 19395-3697 Tehran, Iran

ARTICLE INFO

Article History:

Received 27 August 2020

Accepted 26 November 2020

Published 01 January 2021

Keywords:

Band-gap

Calcination temperature

Gelatin

Nanoparticle

Vanadium oxide

ABSTRACT

The V_2O_5 nanoparticles were synthesized from VCl_3 precursor via a rather facile sol-gel route in gelatin medium followed by calcination at different temperatures of 400, 500 and 600 °C. The prepared samples were studied for their structural, morphological, optical and magnetic properties. The results showed that the synthesized particles consist mainly of crystalline α - V_2O_5 orthorhombic phase. The calcination at higher temperatures caused an increment in the amount of other vanadium oxides minor phases, namely β - V_2O_5 , and also increased the crystallite size from about 22 to 29 nm. The lattice contraction observed on calcination at higher temperatures may be associated to the the lower density of oxygen vacancies. The optical studies revealed the effect of raising the calcination temperature as a red shift in their direct band gap energy from 2.92 to 2.77 eV due to the size effects. The magnetic characterization of the sample calcined at 400 °C demonstrated a weak ferromagnetic behavior with saturation magnetization of about 0.14 emu/g induced probably by the oxygen vacancies

How to cite this article

Mousavi M., Tabatabai Yazdi Sh., Khorrami Gh.H. Structural, Optical and Magnetic Characterization of Vanadium Pentoxide Nanoparticles Synthesized in a Gelatin Medium. J Nanostruct, 2021; 11(1): 105-113. DOI: 10.22052/JNS.2021.01.012

INTRODUCTION

Metal oxide nanomaterials offering many promising applications in different areas of physics, chemistry, biology, medicine and metal science have received considerable attention [1-4]. V_2O_5 is an important multifunctional transition metal oxide owing to its remarkable structural, electrical, chemical, optical, electrochemical and thermochromic properties, along with low cost, bio-compatibility and easy synthesis making it attractive for many applications. It can be used as chemical gas and moisture sensors [5,6], catalysts [7], solar cells [8], super capacitors [9], cathode material in rechargeable Li batteries [10], optoelectronic switches [11], electrochromic and thermochromic devices [12,13].

Bulk V_2O_5 is a diamagnetic semiconductor with the band gap energy of $E_g = 2.2 - 2.3$ eV [14]. It has several polymorphs including the orthorhombic (Pmmn) α - V_2O_5 [15], tetragonal or monoclinic (P21/m) β - V_2O_5 [16,17] and orthorhombic (Pnma) γ - V_2O_5 [18]. The former is the most common phase built up from the $V^{5+}O_5$ square pyramids linked in the layers by sharing their edges and corners. The other two phases can be obtained from α - V_2O_5 one under special conditions of high temperature or pressure [19]. In the report of Filonenko et al. [17], the β - V_2O_5 phase was attained by a high pressure-high temperature method and characterized also as a layered structure of edge-sharing $V^{5+}O_6$ octahedra chains along b axis. β - V_2O_5 is metastable and thermogravimetric studies showed its

* Corresponding Author Email: : shtabatabai@um.ac.ir

transformation to α - V_2O_5 phase upon heating to 370-380 °C under ambient pressure [17]. γ - V_2O_5 phase is also metastable and has been reported to transform easily to α - V_2O_5 through heating at temperatures higher than 340 °C [18]. However, the phase transitions are significantly affected by the sample preparation conditions.

In recent years, the advances in synthesis of V_2O_5 nanostructures have drawn more attention to them. To date, various methods have been employed for their preparation, such as hydrothermal [20], solvothermal [21], sol-gel [22,23], spray pyrolysis [24], precipitation [25], mechanical alloying [26], pulsed laser deposition [27], electron beam evaporation [28] and chemical vapor deposition [29]. Among them, sol-gel may be the most favorable method for preparation of highly pure and well-dispersed homogeneous nanocrystals. It involves mainly hydrolysis of molecular precursor in aqueous solution (sol) resulting in a loose gel with liquid filled pores, comprising either discrete particles or continuous polymer networks, and then removal of the liquid and condensation of the product via heat treatment. There are a lot of reports on the synthesis of different V_2O_5 nanostructures through sol-gel based techniques. However, controlling the growth process to obtain nanocrystals of narrow-sized distribution with uniform morphology is challenging.

In this investigation, we synthesized V_2O_5 nanoparticles through a rather facile sol-gel route in gelatin medium for the first time. Here, gelatin, a natural polymer capable of being readily dissolved in hot water, contains functional groups that can bind to metal ions and acts as a suitable polymerization agent and owing to its expansion upon heating, it also serves as a terminator for nanoparticles growth hindering the particles to come together. The sol-gel process was followed by calcination at different temperatures of 400, 500 and 600 °C. To explore the optimum calcination temperature, the prepared samples were studied for their structural, morphological, optical and magnetic properties.

MATERIALS AND METHODS

Sample synthesis

To synthesize about 2 g of V_2O_5 nanoparticles via a sol-gel route in a gelatin medium, 4 g of gelatin from bovine skin (gelatin type B from Sigma-Aldrich) as a stabilizer was firstly dissolved

in 120 ml of deionized water in a water bath of 40 °C on a hot plate and stirred for about 30 min to achieve a clear solution. Meanwhile, about 3.5 g of vanadium(III) chloride (VCl_3 from Merck with purity of better than 99%) was dissolved in minimum amount of deionized water and stirred for about 30 min. Then, the vanadium solution was gradually added to the gelatin solution while being stirred. The temperature of the water bath raised to 80 °C and kept fixed for about 6 h evaporating the excess solvent until a viscous brownish gel was obtained. The porous xerogel was formed by drying the gel in a oven of 90 °C for 2 h followed by cooling to room temperature. Then, it was powderized using an agate mortar and calcined in air atmosphere at different temperatures of 400, 500 and 600 °C for 10 h using an alumina crucible in a box furnace to remove the gelatin material. Afterwards, it was allowed to be cooled naturally to room temperature to obtain the final nanopowders of green color.

Characterization

The as-synthesized V_2O_5 particles were characterized for structural, morphological, optical and magnetic properties to find out the optimum calcination temperature. Their structural characteristics and phase formation were evaluated by analyzing the X-ray diffraction (XRD) patterns recorded by a D8-Advance Bruker diffractometer using $Cu-K\alpha$ radiation ($\lambda = 1.54056 \text{ \AA}$) in the angular range of $2\theta = 10 - 80^\circ$ in a continuous scan mode with a step size of 0.04° . The XRD profiles were refined by CELREF software working on the basis of the least-square method.

The shape and size of the synthesized particles were studied by transmission electron microscopy (TEM) of the suspensions of the involved powders dispersed in ethanol and deposited over some carbon coated Cu grids using a Philips CM120 TEM system.

For optical characterization, to avoid difficulties in obtaining the UV-Vis absorption spectra of the dispersed samples, the diffuse reflectance spectra (DRS) of dry powders were studied. To do so, the DRS of dry-pressed disks with thickness of less than 1.5 mm from the synthesized powders and the standard material of $BaSO_4$ with the ratio of 1:10 were recorded in the wavelength range of 250 – 1100 nm using an AvaSpec-2048-TEC Avantes spectrometer with AvaLight DH-S deuterium-halogen light source.

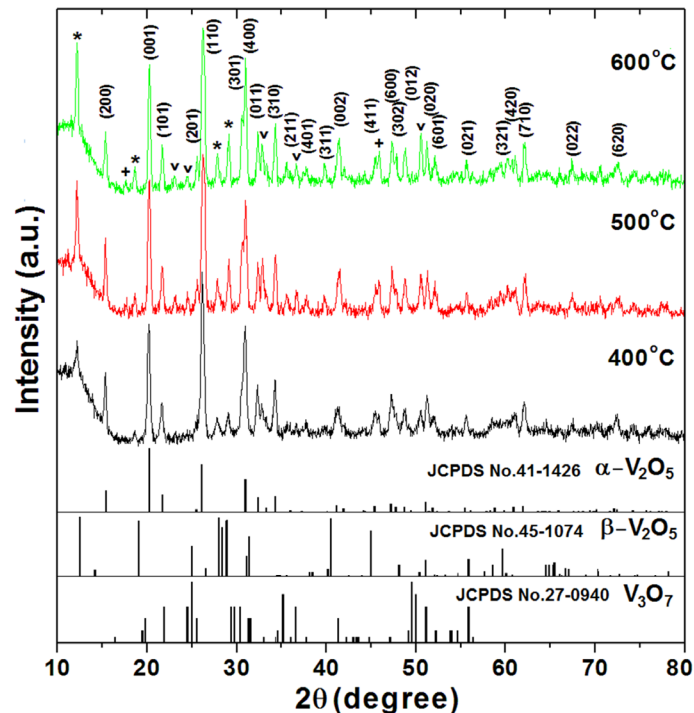


Fig. 1. Room temperature XRD patterns of the as-synthesized particles calcined at different temperatures taken by Cu-K α radiation. The tick marks below the profiles indicate the position of the allowed Bragg reflections belonging to α -V₂O₅, β -V₂O₅ and V₃O₇. The asterisk, vee and plus symbols denote the peaks belonging to β -V₂O₅, V₃O₇ and V₆O₁₃ minor phases, respectively.

The magnetic behavior of the samples were examined through the room temperature magnetization loops measured by a homemade vibrating sample magnetometer (VSM, Meghnatis Daghigh Kavir Kashan Co., Iran) under the applied magnetic fields up to ± 14 kOe.

RESULTS AND DISCUSSION

Structural and morphological analysis

The XRD patterns of the V₂O₅ powders with the calcination temperatures (T_{cal}) of 400, 500 and 600 °C are shown in Fig. 1. All the samples are crystalline; this was expected since it has been reported that the crystallization of V₂O₅ starts upon heat treatment at 300 °C [22]. The sample calcined at 400 °C exhibits predominately the diffraction peaks belonging to α -V₂O₅ orthorhombic phase with Pmmn space group (JCPDS file No. 41-1426) along with some additional sharp peaks at about 12.4, 18.9, 27.9 and 28.8 ° corresponding to (200), (221), (240) and (241) reflections of β -V₂O₅ tetragonal phase (JCPDS file No. 45-1074), respectively. There are also a few peaks of negligible intensity from V₃O₇ monoclinic minor phase with C2/c space group (JCPDS file No. 27-

0940). The coexistence of different vanadium oxides minor phases has been reported for other attempts to synthesize vanadium pentoxide [30-32], as well.

On increasing the calcination temperature, the intensity of the reflections belonging to β -V₂O₅ and V₃O₇ crystalline phases increases and moreover, two additional peaks at 17.8 and 45.8 ° emerge which can be indexed as (002) and (005) characteristic reflections of V₆O₁₃ monoclinic phase with P21/a space group (JCPDS file No. 25-1251). This shows that the heat treatment not only controls the crystallization process, but also results in emergence of more oxygen-rich phases. The calcination at $T_{cal} = 400$ °C provides V and O ions enough mobility to form the crystalline α -V₂O₅. At higher temperatures, as the ions attain more energy, some of α -V₂O₅ unit cells are distorted to form the β -V₂O₅ ones.

The enlarged view of the region around (001) peak (Fig. 2a) reveals a slight shift to higher angles on increasing the calcination temperature. In other words, the interplanar spacing shrinks with the calcination temperature increment. The refined lattice parameters of α -V₂O₅ unit cell

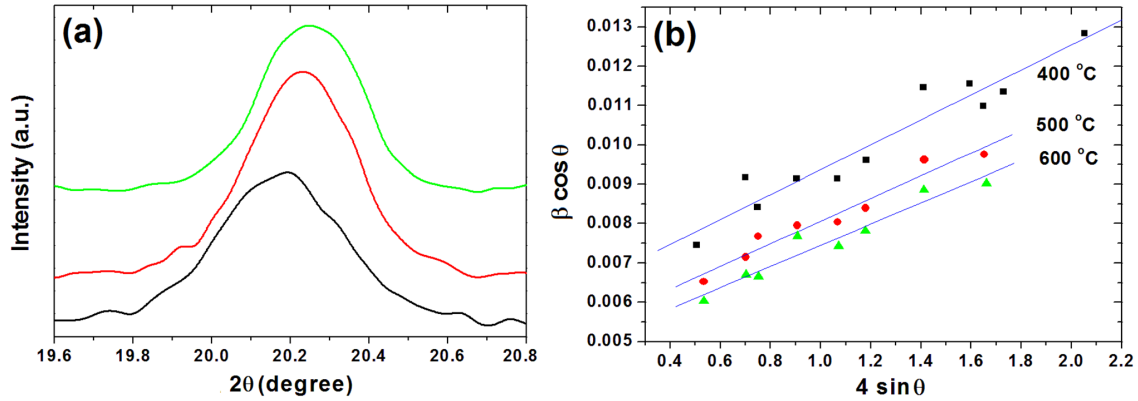


Fig. 2. (a) Enlarged view of $2\theta = 19.6 - 20.8^\circ$ region in XRD patterns, and (b) W-H plots for V_2O_5 nanoparticles calcined at different temperatures.

Table 1. Lattice parameters, crystallite size (D), lattice microstrain (ϵ), dislocation density (δ) and band gap values (E_g) of V_2O_5 nanoparticles calcined at different temperatures (T_{cal}), as well as their particle size evaluated based on the effective mass approximation (D_o).

T_{cal} (°C)	a (Å)	b (Å)	c (Å)	V (Å ³)	D (nm)	ϵ (10 ⁻³)	δ (line/cm ²)	E_g (eV)	D_o (nm)
400	11.511(6)	3.563(3)	4.371(8)	179.328(1)	22.36	3.17	2.00×10^{11}	2.92	35.00
500	11.501(5)	3.561(9)	4.366(7)	178.891(4)	26.71	2.88	1.40×10^{11}	2.85	37.09
600	11.496(5)	3.559(0)	4.365(5)	178.619(0)	29.13	2.69	1.18×10^{11}	2.77	40.13

in the synthesized particles are given in Table 1. The lattice contraction on T_{cal} increment observed also for some other oxide nanoparticles under heat treatment [33-36] can be associated to the decreased density of oxygen vacancies and the consequent local lattice disorders whose probable result may be a shrinkage in the unit cell and/or the presence of the incompletely coordinated ions at the surface of the nanoparticles. The surface ions having dangling bonds form a parallel array of repulsive electric dipoles. These repulsive interdipolar forces decrease on account of the adsorbed oxygen ions at higher temperatures and hence the attractive electrostatic interactions between vanadium and oxygen ions increase resulting in a lattice contraction [36].

Another effect of the calcination temperature is also revealed from the enlarged peaks view in Fig. 2a as a reduction in the width of the diffraction peaks, i.e. a growth in the crystallite size. The Williamson-Hall (W-H) equation was used to determine both the crystallite size (D) and lattice microstrain (ϵ) of the synthesized particles based on the the full width at half maximum (FWHM) of the peaks:

$$\beta \cos \theta = \frac{0.9\lambda}{D} + 4\epsilon \sin \theta \quad (1)$$

where, θ is the diffraction angle of a main reflection, β is FWHM of that peak and λ is the X-ray wavelength, 1.54056 Å. The W-H plots ($\beta \cos \theta$ against $4 \sin \theta$) for the synthesized samples are presented in Fig. 2b. First of all, they exhibit a positive slope indicating the presence of uniform tensile strains in the involved particles. The values of crystallite (grain) size and lattice microstrain obtained from the intercept and slope of the linearly fitted W-H plots, respectively, are listed in Table 1. The synthesized particles are found to be nanocrystalline whose average size increases from 22 to 29 nm upon raising the calcination temperature from 400 to 600 °C. This can be due to presence of oxygen vacancies and the consequent local lattice disorders, again, whose reduction upon increasing the calcination temperature results in growth of the ordered domains. Another reason for the grain growth observed upon increasing T_{cal} has been proposed by Fang et al. [37]: at high temperatures, the ions attain the sufficient energy to diffuse and reside at the suitable lattice sites

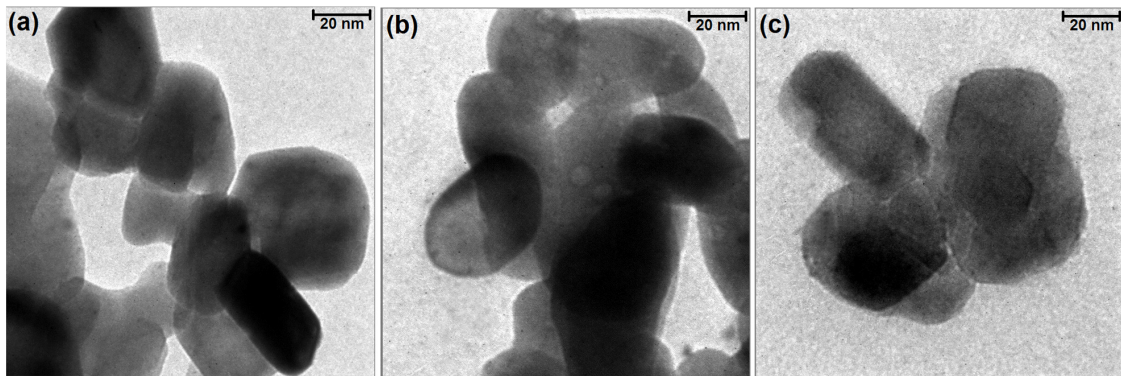


Fig. 3. TEM images of V_2O_5 nanoparticles calcined at (a) 400, (b) 500, and (c) 600 °C.

resulting in larger grains with less surface energy.

The dislocation density being a measure of the defects in the synthesized crystalline particles was evaluated by Williamson and Smallman's relation: $\delta = 1/D^2$ [38]. The calculated δ values tabulated in Table 1, as well as the ϵ values are consistent with the crystallite size variations in the involved nanoparticles. The calcination at elevated temperatures results in less microstrain and dislocation and consequently larger crystallites.

The morphology of the synthesized particles was studied by transmission electron microscopy. The TEM micrographs of the samples with different calcination temperatures in Fig. 3 represent that all the samples consist of individual spherical-like and oval-like nanoparticles of approximately uniform size. The effect of raising T_{cal} is revealed as the increasing number of the oval-shaped particles, probably due to the existence of a mixed phase, as well as a slight increment in their mean size. Regarding Fig. 3, the mean particle size of the samples with T_{cal} of 400, 500 and 600 ° are found to be about 34, 36.5 and 40 nm respectively, i.e. more than the crystallite sizes calculated from the XRD peaks width. This indicates the polycrystalline nature of the synthesized nanoparticles. The nanoparticles size growth with the calcination temperature is in good agreement with other reports (e.g. [39]) and was expected since on temperature increment, the tendency toward the minimum surface energy gives rise to larger particles with the less surface to volume ratio.

Optical properties

The room temperature UV-Vis diffuse reflectance spectra (DRS) of the involved nanoparticles in the wavelength range of 250

- 1100 nm are presented in the inset of Fig. 4a. To use the diffuse reflected data, they were recalculated by Kubelka-Munk (K-M) equation [40]:

$$\frac{K}{S} = \frac{(1-R)^2}{2R} = F(R) \quad (2)$$

Here, K and S are the K-M absorption and scattering coefficients representing the portions of light absorbed and scattered per unit vertical lengths, respectively; They have no direct meaning on their own. R is the ratio of the sample's reflectance to that of the standard (here, $BaSO_4$) and F(R) is the K-M or re-emission function representing the optical absorption behavior. The DRS data of the synthesized particles after K-M treatment are shown in Fig. 4a. As seen, the high values at lower incident photon energies ($h\nu$) decrease and then increase for higher energies, very different from the absorption behavior of thin films (e.g. [24]). The high absorbance (α) at lower energy side of the spectrum hardly originates from the electronic transitions; This should be due to the scattering phenomenon in the involved samples consisting of some nanoparticles with rough surfaces.

The obtained spectra reveal two absorption bands around 1.31 and 2.35 eV almost independent of the calcination temperature. The observed peaks in the absorption spectra do not correspond to the optical band gap energy of the samples. However, occurrence of a sudden raise in the absorbance at a particular incident energy reflects the existence of an optical band gap in the involved particles. Considering a parabolic band structure, the optical band gap energy (E_g) and its type can be estimated using Tauc's relation

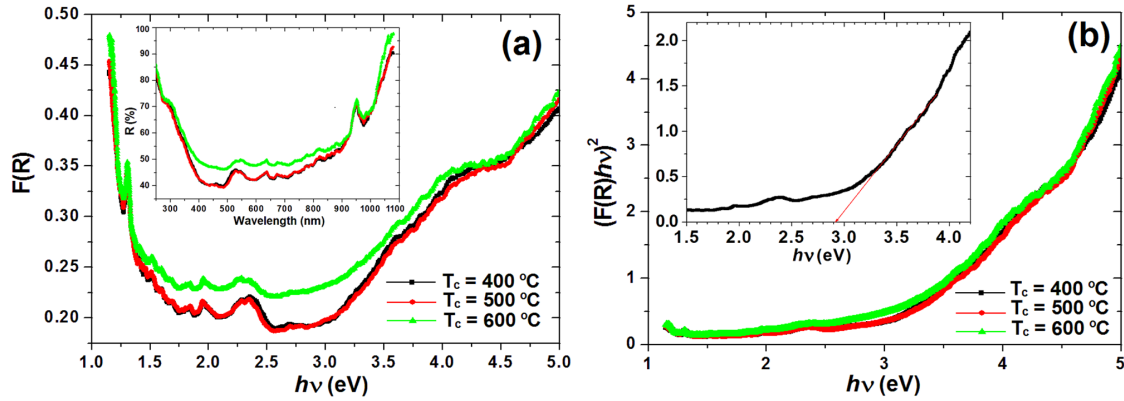


Fig. 4. (a) Optical re-emission function, $F(R)$, and (b) $(Fhv)^2$ versus incident photon energy $h\nu$ for V_2O_5 nanoparticles calcined at different temperatures. The inset shows their diffuse reflectance.

[41]: $(\alpha h\nu)^n = c(h\nu - E_g)$, where c is a constant and index n , depending on the nature of the involving electronic transition, is 2 and 1/2 for the direct and indirect allowed transitions, respectively. Assuming that the samples scatter in a perfectly diffuse manner, the K-M absorption coefficient (K) equals to 2α , so considering S independent of energy [42], one has:

$$(F(R)h\nu)^n = c'(h\nu - E_g) \quad (3)$$

The graphs of $(Fhv)^2$ and $(Fhv)^{1/2}$ versus $h\nu$ were plotted and it was found that the former has the best line fitting revealing that the synthesized nanoparticles are the direct bandgap materials. The direct band gap values were deduced by extrapolating the linear portion of the curves to the energy axis ($F = 0$), as shown in Fig. 4b. Despite the differences in the phases formed in the particles calcined at 400 to 600 °C and their mean size (D'), their optical band gap energies show only a slight difference from 2.92 to 2.77 eV (Table 1). The obtained E_g values are comparable to but more than that reported for the bulk V_2O_5 (2.3 eV, [43]) due to the quantum confinement effect in the synthesized nanoparticles. The decrease observed in E_g values of the involved nanoparticles with the calcination temperature or in other words with the particle size growth is also consistent with the quantum size effect.

Based on the obtained E_g values, the radii of the synthesized nanoparticles (R) were additionally determined using Brus equation based on the effective mass approximation [44]:

$$E_g - E_{gb} = \frac{h^2}{8R^2\mu} - \frac{1.8e^2}{4\pi\epsilon_0\epsilon R} \quad (4)$$

where E_{gb} is the optical band gap energy of the bulk material, μ is the combined effective mass of electrons and holes ($= m_e m_h / (m_e + m_h)$), being equal to $1.99 m_0$ for V_2O_5 , using $m_e = 3.0 m_0$ and $m_h = 5.9 m_0$ [43]; m_0 is the free electron mass), e_0 is the permittivity of free space, and ϵ is the dielectric constant ($\epsilon = 5.9$ for α - V_2O_5 [45]). Considering the spherical-like particles, their size ($D_0 = 2R$) determined by this way are in the range of 35 – 40 nm (Table 1). They are almost the same as the mean particle sizes obtained from TEM images and a bit larger than the mean crystallite sizes obtained from the XRD lines broadenings.

Magnetic properties

The room temperature magnetization (M) of V_2O_5 nanoparticles freshly calcined at 400 °C versus the applied magnetic fields (H) up to ± 14 kOe is shown in Fig. 5. The magnetic loop with a small remanence (0.0056 emu/g) and coercivity (135 Oe) demonstrates a weak ferromagnetic behavior for the involved nanoparticles (see lower inset in Fig. 5). It is notable that the XRD patterns reveal no detectable sign of any magnetic impurity phase. V_2O_5 whose V^{5+} ions ($3d^0$) have no unpaired electrons does not possess intrinsic magnetic moments as well, but a direct connection has been experimentally and theoretically established between the oxygen vacancies and ferromagnetism in this material [46,47]. By density functional theory (DFT) calculations, Xioa et al. [47] predicted that $V_2O_{5-\delta}$ would be a diluted ferromagnet with

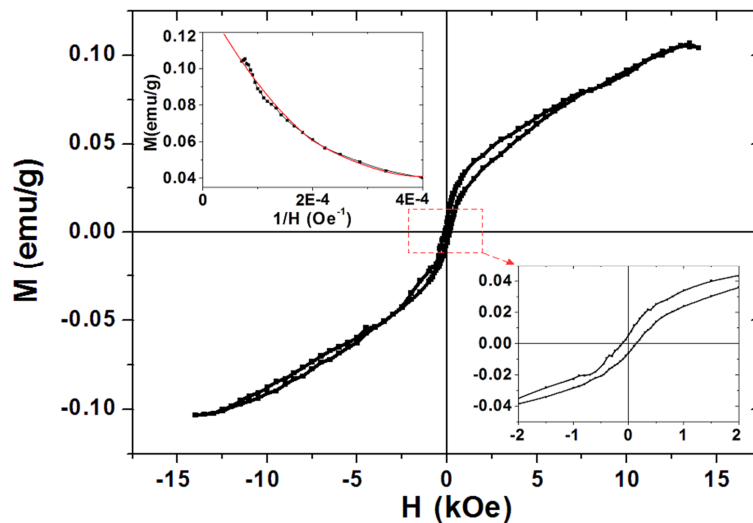


Fig. 5. Room temperature M-H loop of V_2O_5 nanoparticles calcined at 400 °C. The lower inset shows the enlarged view around the origin. The upper inset is the plot of M versus $1/H$; The red line is the fitted second order polynomial function.

magnetic moment of about $2 \mu_B$ /vacancy for $\delta < 0.13$ and $0.19 < \delta < 0.45$.

As seen, the involved nanoparticles are not saturated even under the maximum applied magnetic field of 14 kOe. The saturation magnetization (M_s) of the synthesized nanoparticles was obtained considering the law of approach to magnetic saturation for high magnetic field region [48]:

$$M(H,T) = M_s(T) (1 - a/H - b/H^2) + \chi_{\text{hf}} H \quad (5)$$

Here, the fitting coefficients a and b are related to the contributions of local inhomogeneities and the magnetocrystalline anisotropy, respectively, and the last term is the forced magnetization. As the forced magnetization is negligible below Curie temperature and so at room temperature, one can estimate the M_s value through ignoring the last term and just fitting $M(1/H)$ data by a second order polynomial function, as shown in the upper inset of Fig. 5. Accordingly, the room temperature M_s value of the involved V_2O_5 nanoparticles was found to be 0.139 emu/g being small as compared with some other reported values for nanoparticles of this compound with similar size (2.05 emu/g, [49]), possibly due to the less oxygen vacancies present in the involved sample.

CONCLUSION

The V_2O_5 nanoparticles with different particle sizes ranging from about 34 to 40 nm were synthesized via a simple sol-gel route in gelatin medium followed by calcination at different

temperatures of 400, 500 and 600 °C. The structural characterization shows that the synthesized particles consist mainly of α - V_2O_5 orthorhombic crystallites of 22 – 29 nm and the amount of other vanadium oxides minor phases, namely tetragonal β - V_2O_5 , increases with the calcination temperature. The calcination at elevated temperatures results also in the lattice contraction; this can be due to the decreased density of oxygen vacancies. The optical studies indicate that the involved V_2O_5 nanoparticles are direct band gap semiconductors whose band gap value decreases with calcination temperature from 2.92 to 2.77 eV due to the size effects. The size of the synthesized nanoparticles estimated based on the optical results are in very good agreement with the mean particle sizes obtained by electron microscopy (35 – 40 nm). The V_2O_5 nanoparticles calcined at 400 °C showed a weak ferromagnetism at room temperature with saturation magnetization of 0.139 emu/g owing probably to the small amount of oxygen vacancies present in the sample.

CONFLICT OF INTEREST

The authors declare that there is no conflict of interests regarding the publication of this manuscript.

REFERENCES

1. Chavali MS, Nikolova MP. Metal oxide nanoparticles and their applications in nanotechnology. *SN Applied Sciences*. 2019;1(6).

2. Alavi-Tabari SAR, Khalilzadeh MA, Karimi-Maleh H. Simultaneous determination of doxorubicin and dasatinib as two breast anticancer drugs uses an amplified sensor with ionic liquid and ZnO nanoparticle. *Journal of Electroanalytical Chemistry*. 2018;811:84-8.
3. Karimi-Maleh H, Sheikhshoae M, Sheikhshoae I, Ranjbar M, Alizadeh J, Maxakato NW, et al. A novel electrochemical epinine sensor using amplified CuO nanoparticles and an-hexyl-3-methylimidazolium hexafluorophosphate electrode. *New Journal of Chemistry*. 2019;43(5):2362-7.
4. Miraki M, Karimi-Maleh H, Taher MA, Cheraghi S, Karimi F, Agarwal S, et al. Voltammetric amplified platform based on ionic liquid/NiO nanocomposite for determination of benserazide and levodopa. *Journal of Molecular Liquids*. 2019;278:672-6.
5. Schneider K, Lubecka M, Czapl A. V₂O₅ thin films for gas sensor applications. *Sensors and Actuators B: Chemical*. 2016;236:970-7.
6. Pawar MS, Bankar PK, More MA, Late DJ. Ultra-thin V₂O₅ nanosheet based humidity sensor, photodetector and its enhanced field emission properties. *RSC Advances*. 2015;5(108):88796-804.
7. Mazidi M, Behbahani RM, Fazeli A. Ce promoted V₂O₅ catalyst in oxidation of SO₂ reaction. *Applied Catalysis B: Environmental*. 2017;209:190-202.
8. Arbab EAA, Mola GT. V₂O₅ thin film deposition for application in organic solar cells. *Applied Physics A*. 2016;122(4).
9. Majumdar D, Mandal M, Bhattacharya SK. V₂O₅ and its Carbon-Based Nanocomposites for Supercapacitor Applications. *ChemElectroChem*. 2019;6(6):1623-48.
10. Rao M.C. Vanadium pentoxide cathode material for fabrication of all solid state lithium-ion batteries -a case study. *Res. J. Recent Sci.*, 2013; 2: 67-73.
11. Lu J, Hu M, Tian Y, Guo C, Wang C, Guo S, et al. Fast visible light photoelectric switch based on ultralong single crystalline V₂O₅ nanobelt. *Optics Express*. 2012;20(7):6974.
12. Wei Y, Zhou J, Zheng J, Xu C. Improved stability of electrochromic devices using Ti-doped V₂O₅ film. *Electrochimica Acta*. 2015;166:277-84.
13. Kumar S, Qadir A, Maury F, Bahlawane N. Visible Thermo-chromism in Vanadium Pentoxide Coatings. *ACS Applied Materials & Interfaces*. 2017;9(25):21447-56.
14. Kenny N, Kannewurf CR, Whitmore DH. Optical absorption coefficients of vanadium pentoxide single crystals. *Journal of Physics and Chemistry of Solids*. 1966;27(8):1237-46.
15. Enjalbert R, Galy J. A refinement of the structure of V₂O₅. *Acta Crystallographica Section C Crystal Structure Communications*. 1986;42(11):1467-9.
16. Volkov VL, Golovkin BG, Fedjukov AS, Zainulin YG. *ChemInform Abstract: Synthesis and Properties of the Oxide β-V₂O₅*. *ChemInform*. 1989;20(7).
17. Filonenko VP, Sundberg M, Werner PE, Zibrov IP. Structure of a high-pressure phase of vanadium pentoxide, β-V₂O₅. *Acta Crystallographica Section B Structural Science*. 2004;60(4):375-81.
18. Cocciantelli JM, Gravereau P, Doumerc JP, Pouchard M, Hagenmuller P. On the preparation and characterization of a new polymorph of V₂O₅. *Journal of Solid State Chemistry*. 1991;93(2):497-502.
19. Balog P, Orosel D, Cancarevic Z, Schön C, Jansen M. V₂O₅ phase diagram revisited at high pressures and high temperatures. *Journal of Alloys and Compounds*. 2007;429(1-2):87-98.
20. Mu J, Wang J, Hao J, Cao P, Zhao S, Zeng W, et al. Hydrothermal synthesis and electrochemical properties of V₂O₅ nanomaterials with different dimensions. *Ceramics International*. 2015;41(10):12626-32.
21. Slewa LH, Abbas TA, Ahmed NM. Hydrothermal and solvothermal synthesis of nanorods and 3D (micro/nano) V₂O₅ on macro PSi substrate for pH-EGFET sensors. *Journal of Materials Science: Materials in Electronics*. 2019;30(12):11193-207.
22. Przeźniak-Welenc M, Łapiński M, Lewandowski T, Kościńska B, Wicikowski L, Sadowski W. The Influence of Thermal Conditions on V₂O₅ Nanostructures Prepared by Sol-Gel Method. *Journal of Nanomaterials*. 2015;2015:1-8.
23. Gotić M, Popović S, Ivanda M, Musić S. Sol-gel synthesis and characterization of V₂O₅ powders. *Materials Letters*. 2003;57(21):3186-92.
24. Mousavi M, Kompany A, Shahtahmasebi N, Bagheri-Mohagheghi MM. Study of structural, electrical and optical properties of vanadium oxide condensed films deposited by spray pyrolysis technique. *Advances in Manufacturing*. 2013;1(4):320-8.
25. Rosaiah P, Sandhya GL, Hussain OM. Impedance Spectroscopy and Electrochemical Properties of Nano-Crystalline Vanadium Pentoxide (V₂O₅) Synthesized by Co-Precipitation Method. *Advanced Science, Engineering and Medicine*. 2016;8(2):83-90.
26. Aparna S, Balamurugan S, Fathima TKS, Sreenija SV, Palanisami N. Structural Characterization of High Energy Ball Milled Nanocrystalline Vanadium (V) Oxide (V₂O₅) Powder. *Advanced Science, Engineering and Medicine*. 2017;9(3):188-94.
27. McGraw J.M., Perkins J.D., Hasoon F, Parilla P.A. Pulsed laser deposition of oriented V₂O₅ thin films. *J. Mater. Res.*, 2000; 15: 2249-2265.
28. Thiagarajan S, Thaiyan M, Ganesan R. Physical property exploration of highly oriented V₂O₅ thin films prepared by electron beam evaporation. *New Journal of Chemistry*. 2015;39(12):9471-9.
29. Vernardou D. Using an Atmospheric Pressure Chemical Vapor Deposition Process for the Development of V₂O₅ as an Electrochromic Material. *Coatings*. 2017;7(2):24.
30. Mousavi M, Kompany A, Shahtahmasebi N, Bagheri-Mohagheghi MM. CHARACTERIZATION AND ELECTROCHROMIC PROPERTIES OF VANADIUM OXIDE THIN FILMS PREPARED VIA SPRAY PYROLYSIS. *Modern Physics Letters B*. 2013;27(21):1350152.
31. Le TK, Kang M, Kim SW. Room-temperature photoluminescence behavior of α-V₂O₅ and mixed α-β phase V₂O₅ films grown by electrodeposition. *Materials Science in Semiconductor Processing*. 2019;94:15-21.
32. Su Q, Lan W, Wang YY, Liu XQ. Structural characterization of β-V₂O₅ films prepared by DC reactive magnetron sputtering. *Applied Surface Science*. 2009;255(7):4177-9.
33. Thongtha A, Bongkarn T. Phase Formation and Microstructure of Barium Zirconate Ceramics Prepared Using the Combustion Technique. *Ferroelectrics*. 2009;383(1):33-9.
34. Khan RN, Ali N, Riaz S, Naseem S. Effect of Calcination on Properties of Cobalt Doped ZnO Nanoparticles. *Materials Today: Proceedings*. 2015;2(10):5765-70.
35. Mahía J, Vieiro A, Mira J, Rivas J, López-Quintela MA,

- Oseroff SB. Influence of Calcination Temperature on Lattice Parameters and Particle Size of R_2CuO_4 Compounds (R= Gd, Nd) Prepared by a Sol–Gel Method. *Journal of Solid State Chemistry*. 1996;122(1):25-30.
36. Soosen M.S., Bose L., George K.C. Optical properties of ZnO nanoparticles. *Academic Review*, 2009; 57-65.
37. Fang ZB, Yan ZJ, Tan YS, Liu XQ, Wang YY. Influence of post-annealing treatment on the structure properties of ZnO films. *Applied Surface Science*. 2005;241(3-4):303-8.
38. Williamson GK, Smallman RE. III. Dislocation densities in some annealed and cold-worked metals from measurements on the X-ray debye-scherrer spectrum. *Philosophical Magazine*. 1956;1(1):34-46.
39. Pilban Jahromi S, Pandikumar A, Goh BT, Lim YS, Basirun WJ, Lim HN, et al. Influence of particle size on performance of a nickel oxide nanoparticle-based supercapacitor. *RSC Advances*. 2015;5(18):14010-9.
40. Escobedo-Morales A, Ruiz-López II, Ruiz-Peralta Md, Tepech-Carrillo L, Sánchez-Cantú M, Moreno-Orea JE. Automated method for the determination of the band gap energy of pure and mixed powder samples using diffuse reflectance spectroscopy. *Heliyon*. 2019;5(4):e01505.
41. Tauc J. Optical properties and electronic structure of amorphous Ge and Si. *Materials Research Bulletin*. 1968;3(1):37-46.
42. Escobedo Morales A., Sánchez Mora E., Pal U. Use of diffuse reflectance spectroscopy for optical characterization of un-supported nanostructures. *Rev. Mex. Fis. S*, 2007; 53: 18–22.
43. Lany S. Semiconducting transition metal oxides. *Journal of Physics: Condensed Matter*. 2015;27(28):283203.
44. Brus LE. Electron–electron and electron-hole interactions in small semiconductor crystallites: The size dependence of the lowest excited electronic state. *The Journal of Chemical Physics*. 1984;80(9):4403-9.
45. Das T., Tosoni S., Pacchioni G. Structural and electronic properties of V_2O_5 and MoO_3 bulk and ultrathin layers. *Comp. Mater. Sci.*, 2019; 163: 230-240.
46. Cezar AB, Graff IL, Varalda J, Schreiner WH, Mosca DH. Local order and the dependence of magnetization on Co content in V_2O_5 layered films. *Journal of Applied Physics*. 2015;118(10):103903.
47. Xiao ZR, Guo GY. Structural, electronic and magnetic properties of V_2O_{5-x} : An ab initio study. *The Journal of Chemical Physics*. 2009;130(21):214704.
48. Zhang H, Zeng D, Liu Z. The law of approach to saturation in ferromagnets originating from the magnetocrystalline anisotropy. *Journal of Magnetism and Magnetic Materials*. 2010;322(16):2375-80.
49. Akande AA, Liganiso EC, Dhonge BP, Rammutla KE, Machatine A, Prinsloo L, et al. Phase evolution of vanadium oxides obtained through temperature programmed calcinations of ammonium vanadate in hydrogen atmosphere and their humidity sensing properties. *Materials Chemistry and Physics*. 2015;151:206-14.